

framework cross-linking, the thermal and hydrothermal stabilities of MSU-G silicas are unprecedented among all previously reported mesostructures, regardless of framework composition or structure. In addition to being structurally stable during calcination at 1000°C (compare Fig. 1B), MSU-G silicas are stable in boiling water for >150 hours. In contrast, we find that MCM-41 and other electrostatically assembled silicas with benchmarked hydrothermal stabilities [including framework-stabilized KIT-1 silica mesostructures (20) and the thick-walled SBA-15 family of silicas (21)] become x-ray amorphous and lose accessible framework mesoporosity in <50 hours when subjected to equivalent calcination and boiling.

The combination of a 3D pore network and a vesicle-like morphology, in addition to the remarkable thermal and hydrothermal stability, has important implications for the use of MSU-G silicas in chemical catalysis and molecular separations. Most mesostructured molecular sieves (particularly those prepared through an electrostatic pathway) exhibit framework pore lengths on a micrometer length scale, which is comparable to the length scale of the mesostructured particles themselves. Access to the framework sites can be limited by diffusion along the pore length, particularly in reactions in condensed media. A combined vesicular morphology and 3D pore network allow the average diameter and length of the mesopores within a particle to be more comparable in their dimensions, thus facilitating access. As a first step toward the catalytic applications of such structures, we have incorporated re-

dox-active Ti(IV) and acidic Al(III) centers into the framework of MSU-G silicas (through postsynthesis reactions with titanium isopropoxide and sodium aluminate) without altering the lamellar framework or the vesicular hierarchical structure.

References and Notes

- G. A. Ozin, *Acc. Chem. Res.* **30**, 17 (1997); H. Yang, N. Coombs, G. A. Ozin, *Nature* **386**, 692 (1997); S. Mann *et al.*, *Chem. Mater.* **9**, 2300 (1997).
- S. Schacht, Q. Huo, I. G. Voigt-Martin, G. D. Stucky, F. Schüth, *Science* **273**, 768 (1996).
- H.-P. Lin and C.-Y. Mou, *ibid.*, p. 765.
- S. Oliver, A. Kuperman, N. Coombs, A. Lough, G. A. Ozin, *Nature* **378**, 47 (1995).
- M. Dubois, T. Gulik-Krzywicki, B. Cabane, *Langmuir* **9**, 673 (1993).
- Q. Huo, J. Feng, F. Schüth, G. D. Stucky, *Chem. Mater.* **9**, 14 (1997).
- P. T. Tanev and T. J. Pinnavaia, *Science* **271**, 1267 (1996).
- P. T. Tanev, Y. Liang, T. J. Pinnavaia, *J. Am. Chem. Soc.* **119**, 8616 (1997).
- A. D. Bangham, M. M. Standish, J. C. Watkins, *J. Mol. Biol.* **13**, 238 (1965); G. Sessa and G. Weissmann, *J. Lipid Res.* **9**, 310 (1968).
- F. Auguste, J.-P. Douliéz, A.-M. Bellocq, E. J. Dufourc, *Langmuir* **13**, 666 (1997); J. Oberdisse, O. Regev, G. Porte, *J. Phys. Chem. B* **102**, 1102 (1998); M. Dubois and T. Zemb, *Langmuir* **7**, 1352 (1991); K. L. Herrington, E. W. Kaler, D. D. Miller, J. A. Zasadzinski, S. Chiruvolu, *J. Phys. Chem.* **97**, 13792 (1993); H. Hoffmann, C. Thunig, U. Munkert, H. W. Meyer, W. Richter, *Langmuir* **8**, 2629 (1992).
- G. Porte, *J. Phys. Cond. Matter* **4**, 8649 (1992).
- K. M. McGrath, D. M. Dabbs, N. Yao, I. A. Aksay, S. M. Gruner, *Science* **277**, 552 (1997).
- C. T. Kresge, M. E. Leonowicz, W. J. Roth, J. C. Vartuli, J. S. Beck, *Nature* **359**, 710 (1992); J. S. Beck *et al.*, *J. Am. Chem. Soc.* **114**, 10834 (1992).
- M. Ogawa, *J. Am. Chem. Soc.* **116**, 7941 (1994); Y. Lu *et al.*, *Nature* **389**, 364 (1997).
- F. Linsker and R. L. Evans, *J. Am. Chem. Soc.* **67**, 1581 (1945).
- Q. Huo, R. Leon, P. M. Petroff, G. D. Stucky, *Science* **268**, 1324 (1995).
- MSU-G mesostructures were prepared by the hydrolysis and polymerization of TEOS in a 1:9 (v/v) ethanol:water solution of a neutral $C_{n-2,0}^{n-2,0}$ gemini surfactant under hydrothermal conditions. The molar ratio of each reaction mixture was 1.0 TEOS:0.25 surfactant:4.3 ethyl alcohol:78 H₂O. TEOS was added to the surfactant in the water:ethanol-mixed solvent under rapid stirring for 30 min, and then the mixture was heated at 100°C in an autoclave for 48 hours under static condition. The product was filtered, washed with cold ethanol, and air-dried. Finally, the surfactant was removed from the surfactant-containing product by calcination in air at 650°C for 4 hours or by extraction with hot ethanol.
- V. Alfredsson *et al.*, *J. Chem. Soc. Chem. Commun.* **1994**, 921 (1994).
- P. T. Tanev and T. J. Pinnavaia, *Chem. Mater.* **8**, 2068 (1996).
- R. Ryoo, J. M. Kim, C. H. Shin, J. Y. Lee, *Stud. Surf. Sci. Catal.* **105**, 45 (1997); R. Ryoo *et al.*, *J. Phys. Chem.* **100**, 17718 (1996).
- D. Zhao *et al.*, *Science* **279**, 548 (1998).
- This research was supported by NSF through Chemistry Research Group grant CHE-9633798.

3 August 1998; accepted 13 October 1998.

Large-Scale Nitrogen Oxide Plumes in the Tropopause Region and Implications for Ozone

Dominik Brunner, Johannes Staehelin,* Dominique Jeker

Continuous measurements of nitrogen oxide and ozone were performed from a commercial airliner during 1 year at cruising altitudes below and above the tropopause. The upper tropospheric nitrogen oxides distribution was found to be strongly influenced by large-scale plumes extending about 100 to 1300 kilometers along the flight track. The plumes were frequently observed downwind of thunderstorms and frontal systems, which most probably caused upward transport of polluted air from the continental boundary layer or nitrogen oxide production in lightning strokes, or both. Particularly in summer, average ozone concentrations in the plumes were enhanced compared to the tropospheric background levels.

Nitrogen oxides ($NO_x = NO + NO_2$) in the tropopause region are important in the context of climate forcing, because NO_x is an important factor in photochemical ozone

formation (1) and controls the partitioning between OH and HO_2 radicals (2). Ozone is an efficient greenhouse gas in the upper troposphere (3), and oxidation by hydroxyl radicals (OH) regulates the lifetime of several radiatively and chemically active gases in the atmosphere. The increase in tropospheric O_3 resulting from growing anthropogenic emissions of NO_x and other O_3 precursors is believed to have substantially contributed to climate forcing, mostly in the second half of this century (amounting

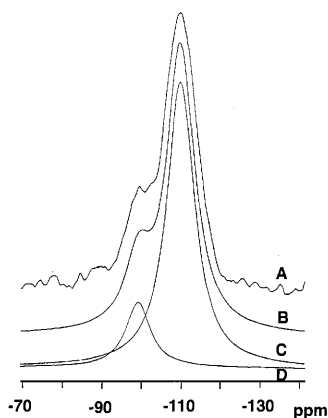


Fig. 4. Curve A is the experimental ^{29}Si MAS NMR spectrum of surfactant-containing MSU-G silica with the gemini surfactant $C_{12}H_{25}NH(CH_2)_2NH_2$ as the structure director. Curve (B) is the sum of the deconvoluted Q^4 (curve C) and Q^3 (curve D) spectral components with relative integral intensities of 6.2:1.0. The single-pulse mode ^{29}Si MAS NMR spectrum was recorded on a Varian VXR-400S spectrometer with a 7-mm zirconia rotor, a spinning frequency of 4 kHz, and a pulse delay of 800 s.

D. Brunner, Atmospheric Composition Research Division, Royal Netherlands Meteorological Institute, 3730 AE De Bilt, Netherlands. J. Staehelin and D. Jeker, Institute for Atmospheric Science, Swiss Federal Institute of Technology, ETH Hoenggerberg HPP, CH-8093 Zurich, Switzerland.

*To whom correspondence should be addressed. E-mail: staehelin@atmos.unm.ethz.ch

REPORTS

to about 25% of the forcing from increasing CO₂ concentrations) (4).

Aircraft emissions are a rapidly growing source of NO_x in the altitude range of 9 to 12 km, which is the cruise altitude of civil airliners. The possible environmental impact of these emissions has received considerable attention in several national and international research programs (5). While the magnitude, distribution, and time dependency of aircraft NO_x emissions are now well quantified, the contribution of other sources, such as convective transport of pollutants from the surface, production of NO by lightning, downward transport from the stratosphere, and recycling from its oxidation products (such as HNO₃, HNO₄, and peroxyacetyl nitrate) is much less certain (6). The individual contributions can be studied with chemical transport models, but until now only a few episodic aircraft measurements were available to verify these model results (7).

The response of O₃ to NO_x increases depends strongly on the chemical composition of the air mass in which NO_x is released (1, 2). In particular, deep convection over polluted areas has been observed to transport large amounts of CO and volatile organic compounds to the upper troposphere (8), which may enhance the efficiency of O₃ production by NO_x considerably. Previous studies, making use of cloud dynamical and chemical box models, suggested that the redistribution of O₃ precursors by convective venting from the polluted boundary layer over the United States can increase O₃ production in the outflow region of thunderstorms (typically at 8 to 12 km) by an order of magnitude compared to the undisturbed atmosphere (9). On the other hand, convective overturning also carries free tropospheric O₃ and NO_x down to Earth's surface, where these compounds are more efficiently removed from the atmosphere (10). Hence, the ongoing debate about the net effect of convection on tropospheric O₃ urgently requires representative measurements to verify the model results that crucially depend on an adequate representation of various trace species including NO_x.

In the NOXAR project (Nitrogen Oxides and Ozone Measurements along Air Routes), an instrument system for the measurement of NO, NO₂, and O₃ was permanently installed in the cargo compartment of a commercial airliner (Swissair, B-747). The system was operated on 540 flights in the Northern Hemisphere (15° to 70°N, 90°W to 120°E) between 5 May 1995 and 13 May 1996. The project aimed to improve understanding of the sources and distribution of NO_x in the tropopause region by taking representative measurements over the course of an entire year. The measurement techniques and the quality of the data have been described elsewhere (11, 12). Because of significant instru-

mental uncertainties in the NO₂ measurements, mainly during the first half of the campaign, NO₂ was additionally calculated from daytime NO and O₃ measurements, assuming a simple photostationary equilibrium between NO, NO₂, and O₃ (13). The NO_x data we present are based on measured NO and calculated NO₂ (NO₂^{*}) concentrations and will therefore be referred to as NO_x^{*}. Meteorological (temperature, wind) and positional data (latitude, longitude, pressure altitude) were obtained from B-747 standard instruments. Additionally, meteorological fields (wind, temperature, geopotential, humidity) from ECMWF analyses (14) were interpolated in time and space to the aircraft positions. Potential vorticity (PV), a dynamical tracer of stratospheric air, was derived from the ECMWF fields and used to separate the measurements into tropospheric and stratospheric samples [PV smaller and larger

than 2 PVU (potential vorticity units), respectively. (1 PVU = 10⁻⁶ m² s⁻¹ K kg⁻¹).

An example of a large-scale NO_x^{*} plume was observed over the United States near the Atlantic coast on 28 August 1995 (Fig. 1). In addition to the extended plume centered at 18:50 UTC (coordinated universal time), a number of sharp NO_x^{*} increases were observed (Fig. 1). Such small-scale peaks were detected on nearly every flight, independent of season, and the meteorological parameters did not change during these events. They were most probably caused by the sampling of exhaust plumes from other aircraft in the flight corridor (15). The highest O₃ concentrations were observed in the lower stratosphere in flight sections a and c (Fig. 1). Shortly after crossing the tropopause from the stratosphere (section d) into the troposphere (section d), NO_x^{*} concentrations started to increase and remained elevated over a dis-

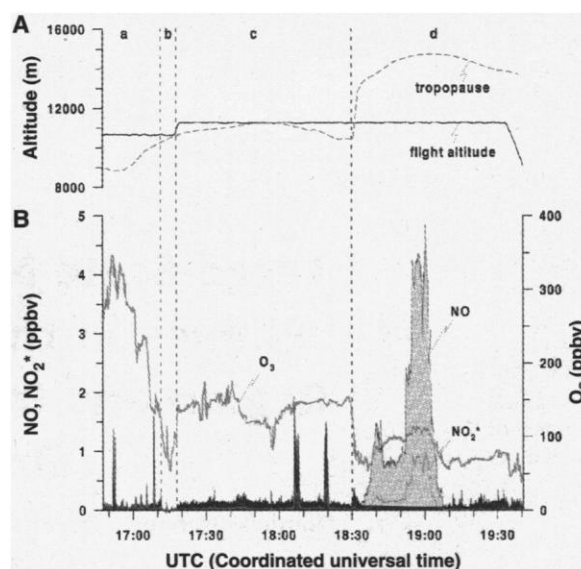
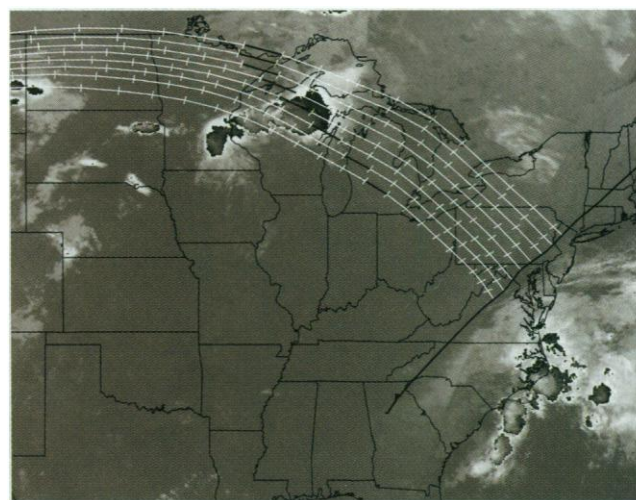


Fig. 1. Time series of measurements of the flight from Zurich to Atlanta from 28 August 1995 showing a large-scale NO_x^{*} plume. (A) Flight level and tropopause altitude (2 PVU level). (B) NO and NO₂^{*} are averaged over 9 s; O₃ is averaged over 4 s. NO₂^{*} is usually a small fraction of NO. The background NO level is shown in dark shades and the plume area above background in light shades. Within the plume, the background is interpolated between the measurements adjacent to the plume.

Fig. 2. Backward trajectories ending in the plume air mass at 18:30 UTC on 28 August 1995 are plotted over a composed infrared satellite image from two overpasses of the NOAA-14 satellite starting at 06:54 (lower right part of the figure) and 08:33 UTC (main part). Trajectories are based on three-dimensional winds from ECMWF analyses. The time step between two ticks on the trajectories is 1 hour. The dark sections on the trajectories mark the positions of the air parcels between 08:00 and 09:00 UTC. Cold (high) parts of the clouds with brightness temperatures below -50°C are highlighted. The black solid line is the flight track of the B-747.



REPORTS

tance of approximately 500 km along the flight track. Ozone was also enhanced relative to the concentrations adjacent to the plume but remained below the stratospheric values observed before. PV and O₃ were anticorrelated within the plume, indicating that the elevated O₃ concentrations were not of stratospheric origin. As shown in Fig. 2, this air mass passed through an area of intense thunderstorm activity southwest of the Great Lakes approximately 10 to 18 hours prior to the measurements, suggesting that the high NO_x* concentrations resulted from convective upward transport of polluted air from the continental U.S. boundary layer. Peak concentrations in the plume of up to 5 parts per billion by volume (ppbv) exceed the typical concentrations of 0.5 to 3.5 ppbv observed at rural surface stations in the eastern United States in late summer (16). Thus, either significant lightning production of NO in the thunderstorm or transport of strongly polluted air from an urban agglomeration most probably contributed to the unusually high concentrations.

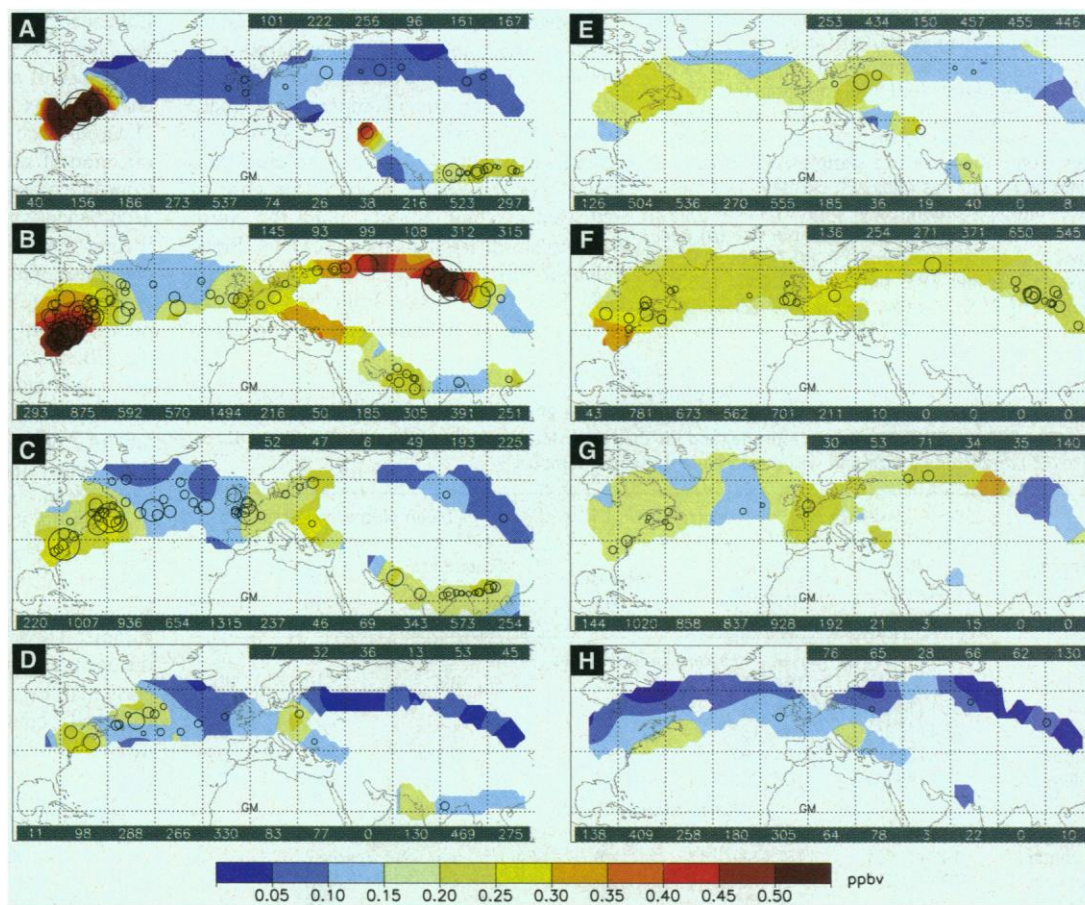
To investigate the origin of such plumes,

we created computer animations for the 70 most pronounced events showing the movement of plume air parcels along their calculated 4-day backward trajectories plotted over the corresponding satellite images of high and cold clouds (infrared images from GOES and METEOSAT available at 3-hour time intervals). An evaluation of these animations suggests the following: (i) In summer, NO_x plumes were observed downwind of convective areas mainly located over the continents. Convective events typically occurred 0.5 to 2 days prior to the measurements (flying directly through active thunderstorms is usually avoided in the flight planning). (ii) During the other seasons, NO_x plumes were observed predominantly downwind of frontal systems. The trajectories then typically followed a path along an upper-level trough associated with a low-pressure system and passed above the cold front connected to the depression. Convective clouds were usually detected ahead of or along the front. (iii) Trajectories based on ECMWF analyses do not resolve the vertical transport of air in convective clouds because of the coarse resolution of the model. Only in a few cases of organized

vertical flow did the model trajectories originate in the continental boundary layer. Satellite images are therefore invaluable for identifying convective activity along the trajectories.

It is difficult to distinguish between NO_x from ground sources and from lightning production, because they are both associated with deep convection and because lightning activity is highly concentrated over the continents (17). On the basis of correlations between NO_x and other tracers of surface emissions, it was concluded in previous studies that a large fraction of upper tropospheric NO_x observed downstream of convective systems over the United States was produced by lightning (8, 18). In the meteorological regime of a frontal passage, however, surface sources dominated over the lightning contribution (18). Little consistent behavior between the enhancements in NO and the changes in other compounds was found in a number of large-scale plumes observed over the equatorial and tropical South Atlantic (19). The sources of NO in these plumes could not be clearly identified, but recycling of NO from reservoir species (mainly HNO₃) and lightning activity were the main contributors.

Fig. 3. Distribution of NO_x* and of large-scale plumes (circles) in the upper troposphere [(A) through (D)] and the lower stratosphere [(E) through (H)] during the four seasons derived from all daytime measurements in the altitude range of 9 to 12 km. From top to bottom: spring [March, April, May (MAM)], summer (JJA), autumn (SON), and winter (DJF). The data were spatially filtered using a two-dimensional Gaussian low-pass filter (17) to suppress features smaller than synoptic scales (less than ~800 km in diameter). Measurements were performed along three major air routes (Zurich-Beijing, Zurich-Bombay-Hong Kong, and Zurich-Atlanta/Boston/Chicago/New York). Each plume event (20) is represented by a circle centered over the midpoint of the plume. The circle areas are proportional to the total amount of NO_x* in the plumes above the background level. They are plotted either in the tropospheric or in the stratospheric part according to where the amount of NO_x* was larger. Numbers at the bottom of each plot indicate the sample size (2-min integrated data) in each 20° longitude section on the flights to the United States and to Bombay and Hong Kong. For the flights to Beijing, these numbers are shown in the top right of each plot. Data gaps indicate areas where only measurements from a single flight or no daytime measurements were available.



The data coverage varies considerably for the following reasons: (i) Spatial and seasonal differences in the average tropopause level. (ii) Fraction of flights performed during the day. Especially in winter, large parts of the flights were at night. (iii) Instrument problems, mainly in June, December, and January. (iv) Flight planning.

The influence of large-scale plume events (20) on the distribution of NO_x* in the upper troposphere and the lower stratosphere is illustrated in Fig. 3. In winter, the tropospheric pattern is similar to that observed in the strato-

sphere but large differences are seen in the other seasons. For example, average NO_x* concentrations in the lower stratosphere over the North Atlantic Ocean exceed the tropospheric values by about 40 pptv (autumn) to 80 pptv (spring and summer). In contrast, upper tropospheric concentrations over the continents may strongly exceed the corresponding stratospheric values during the warm seasons. These differences are related to large-scale plumes that more frequently occurred below the tropopause. Some 11.8% of all tropospheric samples (PV < 2 PVU) in midlatitudes (40° to 60°N) of the entire year, compared with only 3.5% of the stratospheric samples, were obtained within large-scale plumes (21).

By contrasting the concentrations with and without the existence of large-scale plumes averaged over a given area and time period, a rough estimate of their contribution to the NO_x* abundance in the upper troposphere can be calculated (Table 1). The values calculated in this way should be regarded as a lower limit of the combined effect of lightning activity and convective transport, because only the more recent and larger plumes could be clearly distinguished from the background. A considerable increase on the order of 80% is calculated over eastern North America in summer when large-scale plumes are included, whereas over the North Atlantic, the increase is comparatively small. In autumn and winter, however, substantial differences with and without plumes are found over the ocean, probably because of increased cyclonic activity along the North Atlantic storm track in these seasons. Since much of this activity occurred offshore the U.S. East Coast away from large surface sources (Fig. 3), lightning activity appears to

be an important source of NO_x to the North Atlantic region in autumn and winter. The smallest differences were found over the North Atlantic in spring, possibly because convective activity is suppressed by the relatively cold ocean. The large increase over the eastern United States in spring is based on few observations and probably overestimates typical values in this season.

In order to study the effect of the plumes on tropospheric O₃ (Fig. 4), we separated all observations over the eastern United States (50° to 80°W, 30° to 60°N, 9 to 12 km altitude) below the tropopause into two groups according to their location inside (class P) or outside a plume (class NP). In summer, the mean O₃ concentration in class P (88.7 ppbv) was 9.8 ppbv higher than in class NP (78.9 ppbv) (significant at the 99.9% level, using a two-sided Wilcoxon rank sum test). Downward mixing of air from the stratosphere is unlikely to be the reason for this difference. This process would be expected to increase not only O₃ but also potential vorticity. However, with respect to PV the two classes were similar. In summer, PV was even somewhat reduced in class P (0.64 PVU) compared to class NP (0.76). Enhanced photochemical O₃ production in the plumes is a more likely explanation. The difference of about 10 ppbv is comparable to chemical box model calculations of the total O₃ production within the first 24 hours after injection of surface pollutants into the upper troposphere by thunderstorms (9). It is also in accordance with maximum O₃ increases following episodic lightning emissions of NO calculated with a mesoscale chemical transport model (22). In the other seasons, when photochemistry is expected to be less active, the difference in O₃ between class P and NP was much smaller. For example in autumn, mean O₃ values in class P and NP were 57.1 and 54.7 ppbv, respectively, while PV values were nearly the same (0.69 PVU in class P and 0.68 in class NP).

The high NO_x concentrations observed in large-scale plumes thus appear to have a significant and measurable influence on upper tropospheric O₃ concentrations, especially in summer. However, further characterization of the chemical composition of such plumes—in particular by measuring CO, hydrocarbons, carbonyl compounds, and peroxides—is needed to better quantify this effect.

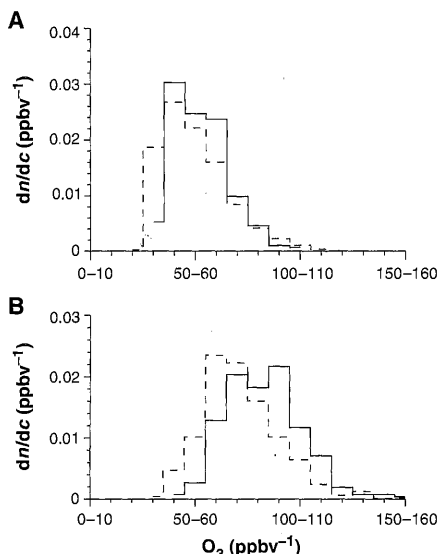


Fig. 4. Density function of the upper tropospheric O₃ (PV < 2PVU) over the eastern United States (30° to 60°N, 50° to 80°W, 9 to 12 km) (A) in autumn and (B) in summer. *n(c)* is the accumulation function counting the number of samples in the O₃ concentration range $[-\infty, c]$, normalized by the total number of samples. Solid lines indicate samples within large-scale NO_x* plumes (class P). Dashed lines indicate samples outside the plumes (class NP). Mean values of O₃, PV, and sample size (*n*) per class and season: (Summer) P: 88.7 ppbv, 0.637 PVU (521); NP: 78.9 ppbv, 0.762 PVU (953). (Autumn) P: 57.1 ppbv, 0.689 PVU (304); NP: 54.7 ppbv, 0.680 PVU (1354).

Table 1. NO_x* concentrations in the upper troposphere (PV < 2PVU) over the eastern United States (35° to 60°N, 50° to 80°W, 9 to 12 km altitude) and for the North Atlantic region (40° to 65°N, 10° to 40°W, 9 to 12 km altitude), with and without large-scale plume samples.

Season	Average NO _x * concentration†			Mean plume properties		
	With plumes (pptv)	Without plumes (pptv)	Increase‡ (%)	Frequency§ (number 10 ⁻⁴ km ⁻¹)	Size (km)	Conc. (pptv)
<i>Eastern United States</i>						
Spring	589 (241)	184 (137)	220	8.5	510	1122
Summer	361 (1442)	200 (981)	81	10.1	315	704
Autumn	224 (1635)	147 (1377)	53	5.2	303	639
Winter	155 (215)	124 (187)	25	6.3	205	359
Full year	301 (3533)	167 (2682)	81	7.5	321	724
<i>North Atlantic Region</i>						
Spring	69 (485)	69 (485)	0	0	—	—
Summer	142 (1223)	132 (1175)	8	1.1	352	398
Autumn	105 (1105)	81 (1034)	29	2.8	232	453
Winter	111 (376)	96 (339)	15	4.5	218	247
Full year	115 (3189)	101 (3033)	14	1.9	255	387

†The sample size is shown in parentheses. Given the speed of the aircraft of about 245 m/s, each 2-min integrated sample represents a flight leg of about 29.4 km. ‡Percent increase, calculated by taking the difference between the concentrations with and without plumes and dividing this by the concentration without plumes. §Spatial frequency in 10⁻⁴ km⁻¹, that is, the number of individual plumes observed per 10,000 km of flight distance.

References and Notes

1. P. J. Crutzen, *J. Geophys. Res.* **76**, 7311 (1971); S. Liu et al., *ibid.* **92**, 4191 (1987); G. P. Brasseur, J.-F. Müller, C. Granier, *ibid.* **101**, 1423 (1996); D. D. Davis et al., *ibid.*, p. 2111.
2. P. O. Wennberg et al., *Science* **279**, 49 (1998).
3. A. A. Lacis, D. J. Wuebbles, J. A. Logan, *J. Geophys. Res.* **95**, 9971 (1990); G. J. Roelofs, J. Lelieveld, R. van Dorland, *ibid.* **102**, 23389 (1997).
4. Intergovernmental Panel on Climate Change, *Climate Change 1994: Radiative Forcing of Climate Change*

Discovery of a Low-Mass Brown Dwarf Companion of the Young Nearby Star G 196-3

Rafael Rebolo,* María R. Zapatero Osorio, Santiago Madruga, Víctor J. S. Béjar, Santiago Arribas, Javier Licandro

A substellar-mass object in orbit at about 300 astronomical units from the young low-mass star G 196-3 was detected by direct imaging. Optical and infrared photometry and low- and intermediate-resolution spectroscopy of the faint companion, hereafter referred to as G 196-3B, confirm its cool atmosphere and allow its mass to be estimated at 25^{+15}_{-10} Jupiter masses. The separation between the objects and their mass ratio suggest the fragmentation of a collapsing cloud as the most likely origin for G 196-3B, but alternatively it could have originated from a protoplanetary disc that has been dissipated. Whatever the formation process was, the young age of the primary star (about 100 million years) demonstrates that substellar companions can form on short time scales.

Direct imaging searches for brown dwarfs and giant planets around stars explore a range of physical separations complementary to that of radial velocity measurements and provide key information on how substellar-mass companions are formed. Any companion uncovered by an imaging technique can be further investigated by spectroscopy, which allows information about its atmospheric conditions and evolutionary status to be obtained. So far, only one unambiguous brown dwarf companion to a star has been imaged (1) and subsequently investigated in detail (2–4). Young, nearby, cool dwarf stars are ideal targets of searches for substellar-mass companions (brown dwarfs and giant planets) using direct imaging techniques, because (i) young substellar objects are considerably more luminous when undergoing the initial phases of gravitational contraction (5–7) than at later stages; (ii) stars in the solar neighborhood (that is, within 50 pc of the sun) allow the detection of faint companions at physical separations of several tens of astronomical units; and (iii) cool stars are among the least luminous stars, which favors full optimization of the dynamic range of current detectors to achieve detection of extremely faint companions by means of narrow-band imaging techniques at red wavelengths.

Using x-ray emission as an indicator of youth (8–10), we have selected a number of late-type stars (K and M spectral classes) in the solar neighborhood, of which we have obtained deep images (down to a limit of about 19 magnitudes in the *I*-band filter at 880 nm) with narrow-band filters (11) centered at 740 and 914 nm (with a bandwidth of 10 nm). The survey is being conducted at the

0.8-m telescope of the Instituto de Astrofísica de Canarias (IAC80) at the Teide Observatory (OT) on Tenerife with a 1024 pixel by 1024 pixel charge-coupled device (CCD). One pixel of this detector projects 0.432 arc sec on the sky. The two narrow filters allow effective discrimination of faint red objects at separations larger than three to four times the full width at half maximum of the point source response, which was on average close to 1.5 arc sec for the first 52 targets of the program. Here we report on the discovery of a very red companion to the high-proper-motion M-class dwarf star G 196-3. The observations were performed on 25 January 1998. A comparison of the images taken at different wavelengths showed that a faint red companion was present at 16.2 arc sec southwest of the star (position angle = 210°; see Fig. 1). We have named this companion G 196-3B. Further optical *R* (660 nm) and *I* broad-band photometry (Table 1) was obtained at the 1-m Optical Ground Station (OGS) telescope on 19 March 1998, whereas infrared *J*-band (1200 nm) and *K*-band (2200 nm) data (Table 1) were collected at the 1.5-m Carlos Sánchez Telescope (TCS) on 24 March 1998. Both telescopes are located at the OT.

Inspection of the second Palomar Observatory Sky Survey red plates (obtained from the Space Telescope Science Institute Digitized Sky Survey) provides a 2σ detection of G 196-3B at the position expected for a proper motion (12) common with that of G 196-3. Images in the *I* band taken with the imager spectrograph (ALFOSC) at the 2.5-m Nordic Optical Telescope (NOT) at the Roque de los Muchachos Observatory (ORM) on 16 February 1998 (with a pixel size of 0.187 arc sec) and with HIRAC on 3 June 1998 (pixel size, 0.109 arc sec) confirm that the faint object has a proper motion ($\mu_{\alpha\cos\delta} = -0.5 \pm 0.1$ arc sec year⁻¹, $\mu_{\delta} = -0.3 \pm 0.1$ arc sec

and an Evaluation of the IPCC IS92 Emission Scenarios, J. T. Houghton et al., Eds. (Cambridge Univ. Press, Cambridge, 1995).

5. U. Schumann, *Atmos. Environ.* **31**, 1723 (1997); U. Schumann, Ed., *Air Pollution Research Report 58*. Publication EUR 16978 EN (Office for Official Publication of the European Communities, Luxembourg, 1996); R. R. Friedl, Ed., *NASA Reference Publication 1400* (NASA, Greenbelt, MD, 1997); G. P. Brasseur et al., *Atmos. Environ.* **32**, 2329 (1998).
6. D. S. Lee et al., *Atmos. Environ.* **31**, 1735 (1997).
7. L. K. Emmons et al., *ibid.*, p. 1851.
8. R. R. Dickerson et al., *Science* **235**, 460 (1987).
9. K. E. Pickering et al., *J. Geophys. Res.* **95**, 14049 (1990); K. E. Pickering et al., *ibid.* **97**, 17985 (1992).
10. J. Lelieveld and P. J. Crutzen, *Science* **264**, 1759 (1994).
11. P. Dias-Lalcaca, D. Brunner, W. Imfeld, W. Moser, J. Staehelin, *Environ. Sci. Technol.*, **32**, 3228 (1998).
12. D. Brunner, thesis, ETH Zurich, Zurich, Switzerland (1998).
13. A simple photostationary state equilibrium results from the following reaction cycle: $\text{NO} + \text{O}_3 \rightarrow \text{NO}_2 + \text{O}_2$ (1); $\text{NO}_2 + \text{h}\nu \rightarrow \text{NO} + \text{O}$ (2); $\text{O} + \text{O}_2 + \text{M} \rightarrow \text{O}_3 + \text{M}$ (3) and is given by

$$[\text{NO}_2] = \frac{k_1[\text{NO}][\text{O}_3]}{J_{\text{NO}_2}}$$

where k_1 is the rate constant of reaction (1) and J_{NO_2} is the rate of the photolysis of NO_2 in reaction (2). The photolysis rate J_{NO_2} was calculated for clear-sky conditions only. The uncertainty in the calculation of NO_2 adds to the uncertainty in total NO_x by not more than 20%, because on average, NO_2 was only a minor fraction (20 to 30%) of total NO_x at 9 to 12 km altitude. Nitrogen oxides values derived from measured NO_2 concentrations were 33 pptv higher, on average, than those calculated from photostationary state NO_2 (11). Given the NO_x concentration averaged over all measurements between December 1995 to May 1996 of 172 pptv, this represents a difference of about 20%.

14. ECMWF (European Centre for Medium-Range Weather Forecast) model at T213/L31 resolution—that is, with 31 vertical layers and 0.75° by 0.75° horizontal resolution.
15. H. Schlager et al., *J. Geophys. Res.* **102**, 10739 (1997).
16. D. D. Parrish et al., *ibid.* **98**, 2927 (1993).
17. C. Price, J. Penner, M. Prather, *ibid.* **102**, 5929 (1997); H. Levy II, W. J. Moxim, P. S. Kasibhatla, *ibid.* **101**, 22911 (1996).
18. W. T. Luke, R. R. Dickerson, W. F. Ryan, K. E. Pickering, L. J. Nunnermaker, *ibid.* **97**, 20647 (1992).
19. S. B. Smyth et al., *ibid.* **101**, 24165 (1996).
20. We define a large-scale plume as the sequence of at least four 2-min integrated NO_x samples that show an average increase relative to the background of at least 0.1 ppbv. The background level during a plume event was simply obtained by linear interpolation between the concentrations adjacent to the plume (Fig. 1). Given the (true air) speed of the aircraft of 250 m/s, four samples correspond to a flight leg of 120 km. A difference of 0.1 ppbv is well above the noise of the measurement (11) and represents a significant increase above background levels of typically 70 to 200 pptv (Table 1).
21. Using a higher PV value of 4 PVU for the tropopause definition, the fraction of samples obtained within plumes is 10.4% and 1.6% for the tropospheric and stratospheric samples, respectively. Thus, the probability to observe a large-scale plume rapidly decreases in the stratosphere.
22. F. Flåtøy and Ø. Hov, *J. Geophys. Res.* **102**, 21373 (1997).
23. The NOXAR project was funded by the Swiss Federal Civil Aviation Authority (BAZL). We thank Swissair for the generous support and ECO Physics Inc. for the design of the instrumentation and the assistance during the measurements. We also acknowledge H. Wernli and M. Bourqui for the trajectory calculations and R. Luethi for providing data from his archive of satellite images, which were both of great help for the interpretation of the measurements.

20 July 1998; accepted 14 October 1998

Instituto de Astrofísica de Canarias, E-38200 La Laguna, Tenerife, Canary Islands, Spain.

*To whom correspondence should be addressed. E-mail: rrl@lliac.es